Resource

Structure

Single-Unit Imaging of Membrane Protein-Embedded Nanodiscs from Two Oriented Sides by High-Speed Atomic Force Microscopy

Graphical Abstract

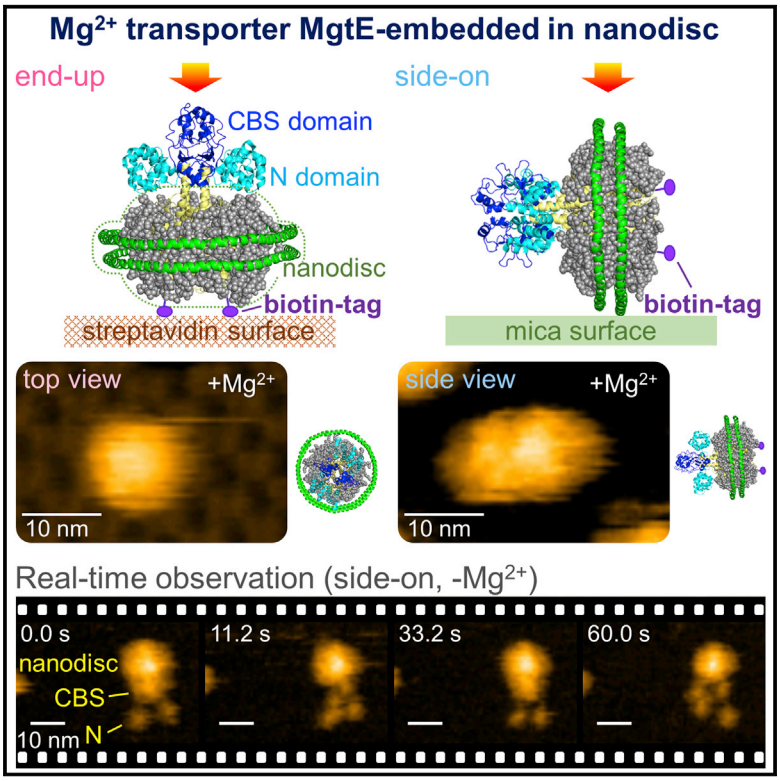

Highlights

- Membrane protein-embedded nanodiscs were used for high-speed (HS)-AFM observation
- Nanodiscs in an end-up and side-on orientation were observed by HS-AFM in real time
- HS-AFM combined with nanodiscs is a powerful tool for membrane protein dynamics

Authors

Takamitsu Haruyama, Yasunori Sugano, Noriyuki Kodera, ..., Yoshiki Tanaka, Hiroki Konno, Tomoya Tsukazaki

Correspondence

hkonno@se.kanazawa-u.ac.jp (H.K.), ttsukazaki@mac.com (T.T.)

In Brief

Haruyama et al. established a procedure for the observation of membrane proteins in nanodiscs by high-speed AFM in real time. Using the two-dimensional crystal of streptavidin as well as mica as a solid support surface, dynamic structural changes of membrane proteins in the lipid environment were visualized from two distinct angles.

Haruyama et al., 2019, Structure 27, 152–160
January 2, 2019
https://doi.org/10.1016/j.str.2018.09.005

CellPress

CellPress

Structure
Resource

Single-Unit Imaging of Membrane Protein-Embedded Nanodiscs from Two Oriented Sides by High-Speed Atomic Force Microscopy

Takamitsu Haruyama,[1,4] Yasunori Sugano,[1,4] Noriyuki Kodera,[2] Takayuki Uchihashi,[3] Toshio Ando,[2] Yoshiki Tanaka,[1] Hiroki Konno,[2,*] and Tomoya Tsukazaki[1,5,*]

[1]Graduate School of Science and Technology, Nara Institute of Science and Technology, Nara 630-0192, Japan
[2]Nano Life Science Institute (WPI-NanoLSI), Kanazawa University, Kanazawa 920-1192, Japan
[3]Department of Physics, Nagoya University, Nagoya 464-8602, Japan
[4]These authors contributed equally
[5]Lead Contact
*Correspondence: hkonno@se.kanazawa-u.ac.jp (H.K.), ttsukazaki@mac.com (T.T.)
https://doi.org/10.1016/j.str.2018.09.005

SUMMARY

Membrane proteins play important roles in various cellular functions. To analyze membrane proteins, nanodisc technology using membrane scaffold proteins allows single membrane protein units to be embedded into the lipid bilayer disc without detergents. Recent advancements in high-speed atomic force microscopy (HS-AFM) have enabled us to monitor the real-time dynamics of proteins in solution at the nanometer scale. In this study, we report HS-AFM imaging of membrane proteins reconstituted into nanodiscs using two membrane protein complexes, SecYEG complex and MgtE dimer. The observed images showed single particles of membrane protein-embedded nanodiscs in an end-up orientation whereby the membrane was fixed parallel to the supporting solid surface and in a side-on orientation whereby the membrane plane was vertically fixed to the solid surface, enabling the elucidation of domain fluctuations in membrane proteins. This technique provides a basic method for the high-resolution imaging of single membrane proteins by HS-AFM.

INTRODUCTION

Many membrane proteins, including drug targets, show inherent activity when properly embedded in specific lipid bilayers. Previous atomic force microscopy (AFM) studies of membrane proteins have employed lipid bilayers spread onto the measurement surface; these lipid bilayers have been prepared from extracted cell membrane fractions or membrane protein-reconstituted liposomes (Bahatyrova et al., 2004; Fotiadis et al., 2003; Ruan et al., 2017; Seelert et al., 2000; Shibata et al., 2010). In some cases, purified membrane proteins solubilized by detergent were directly reconstituted into the supported lipid bilayer onto a supporting solid surface, such as mica and glass (Milhiet et al., 2006; Sumino et al., 2017). Therefore, the orientation of AFM observations for membrane protein dynamics is fixed to only one side (Figure S1A). To overcome this limitation, a monitoring system that can be used to visualize both sides of the membrane is needed for dynamic analyses of certain membrane proteins (Figures S1B and S1C). For example, in many membrane proteins, such as those involved in signal transduction, functional domains on both sides undergo mutual structural changes. Moreover, steric hindrance due to the large size of precursor substrate proteins may prevent protein translocation across the spread membrane. Hence, sufficient space on both sides is necessary to monitor the movement of precursor proteins and evaluate conformational changes in domains on both sides simultaneously. Nanodiscs stably hold the disc-like lipid bilayer with minimal diffusion of the lipids, and provide sufficient space on both sides of the membrane when placed in a side-on orientation (Rouck et al., 2017; Bayburt et al., 2002). Additionally, since nanodiscs can stably retain one functional unit of the membrane protein embedded in the membrane, they are suitable for single-molecule dynamic observation in real time by high-speed (HS)-AFM (Kodera et al., 2010; Miyagi et al., 2016; Shibata et al., 2017; Uchihashi et al., 2011). Single-unit imaging of membrane protein-embedded nanodiscs loaded onto solid surfaces may be achieved from various orientations using HS-AFM under appropriate conditions. Here, two membrane proteins, i.e., the protein-conducting channel SecYEG (Tanaka et al., 2015) and Mg^{2+} transporter MgtE (Hattori et al., 2007), were embedded into nanodiscs and observed by HS-AFM from two oriented sides.

The evolutionarily conserved SecY/SecE/SecG membrane protein complex (SecYEG) forms a complex with the cytosolic motor SecA ATPase to drive protein translocation (du Plessis et al., 2011; Rapoport et al., 2017; Tsirigotaki et al., 2017). The proton-driven motor SecDF also facilitates protein translation at the extracytoplasmic side (Tsukazaki, 2018), and the minimum necessary protein translocation activity can be achieved only by SecA and SecYEG embedded in the lipid bilayer (Akimaru et al., 1991). Therefore, we previously determined the crystal structures of SecYEG and SecA from *Thermus thermophilus*, a

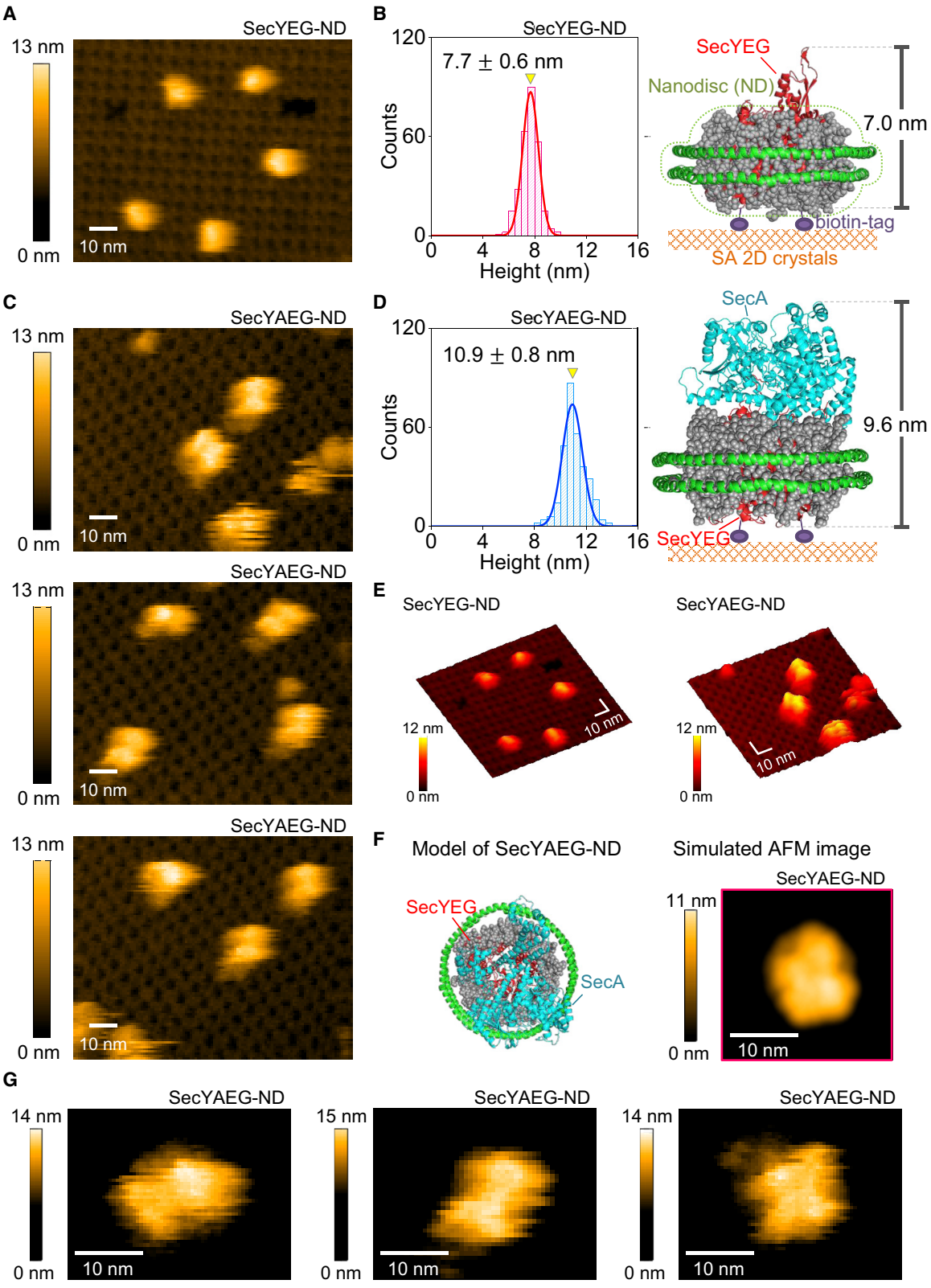

(legend on next page)

thermophilic bacterium (Tanaka et al., 2015; Tsukazaki et al., 2008; Vassylyev et al., 2006), and demonstrated that the SecY-A/SecE/SecG complex (SecYAEG), which includes the fusion protein SecY-SecA, retains the ability to mediate protein transport (Sugano et al., 2017). Moreover, the single-unit SecYAEG complex embedded in a nanodisc (SecYAEG-ND) is strongly associated with a precursor substrate protein (Sugano et al., 2017; Taufik et al., 2013).

RESULTS

SecYEG-NDs and SecYAEG-NDs in the End-Up Orientation

In this study, we first used HS-AFM to observe the SecYEG-reconstituted nanodiscs (SecYEG-NDs) on mica surfaces but could not distinguish the orientation of the nanodiscs, mainly owing to the small size of the observed spherical particles, with diameters of 10 nm, as well as nonspecific binding. Hence, we prepared samples in which all spherical SecYEG-NDs were in the end-up orientation. Purified SecYEG was labeled with biotin at two positions on the periplasmic loops using a double-cysteine mutant (Figure S2), embedded in nanodiscs, and anchored onto the two-dimensional crystal of streptavidin (Yamamoto et al., 2009) (Figure 1A). The nanodiscs were presumed to be oriented as shown in Figure 1B (right). HS-AFM observations showed the presence of ~10-nm spherical objects on the two-dimensional crystal of streptavidin (Figures 1A and 1E [left]). The average height of the spherical molecule (7.7 ± 0.6 nm; n = 277, 277 molecules) was consistent with the height of SecYEG estimated from the crystal structure (Tanaka et al., 2015), suggesting that the observed particles represented SecYEG in the nanodiscs (SecYEG-NDs) (Figure 1B). Next, we observed SecYAEG-NDs and found that the average height (10.9 ± 0.8 nm; n = 305, 305 molecules) was 3.2 nm greater than that of SecYEG-NDs, possibly due to the additional SecA region. This is consistent with the expected height based on the crystal structure (Zimmer et al., 2008) (Figures 1C–1E [right]). Images of SecYAEG-NDs showed round X shapes, similar to the simulated AFM image from the crystal structure (Figure 1F), suggesting that the X-shaped particles are the domains of SecA. Close-up observations indicated that each SecA transitioned among several different conformations, as partially shown in structural analyses (Chatzi et al., 2014) (Figure 1G). Although the differences in SecA particles may reflect the functional and structural changes in solution, we could not clearly distinguish each domain of SecA. Notably, the images showed high resolution, particularly considering that SecA particles did not directly interact with the supporting surface but were positioned on the nanodisc apart from the surface. If we introduced at least three cysteine residues per unit or used shorter biotin-maleimide reagents for fixation to reduce the fluctuation of nanodiscs, we would obtain higher-resolution images. Thus, we established a procedure in which biotin-labeled SecYEG-NDs and SecYAEG-NDs were anchored onto the two-dimensional streptavidin surface in the end-up orientation. Moreover, after biotin labeling via introduced cysteines, we can use HS-AFM as an imaging technique to evaluate membrane-embedded proteins from arbitrary orientations.

SecYAEG-NDs in the Side-On Orientation

To explore the samples from another angle, we observed the SecYAEG-NDs adsorbed on a mica surface. Unexpectedly, we found similarly shaped particles in the same orientation. Each particle consists of one small and one large elliptically shaped object, both of which were clearly distinguishable based on cleavage (Figure 2A). The particle shapes are essentially consistent with the simulated AFM image from the crystal structure, indicating that the SecYAEG-NDs are immobilized with a side-on orientation on the mica surface (Figures 2B and 2C). Furthermore, to reliably confirm the orientation, mixed samples of SecYAEG-NDs with streptavidins were observed on the mica surface (Figure 2D). Compared with the condition without streptavidin, the HS-AFM image showed two additional smaller particles (size of ~5 nm) attached to the side of the large elliptical molecule, implying that the large and small particles correspond to the SecYEG-ND and soluble SecA regions, respectively. Previous AFM studies have shown that membrane protein-embedded nanodiscs are immobilized with the end-up orientation on mica (Koch et al., 2016; Zocher et al., 2012). In our case, the flexibility of SecA and the biotin label may hamper the close interaction between the mica surface and lipid bilayer. Our observations demonstrate the presence of SecYAEG-NDs in the side-on orientation on the mica surface and SecYAEG-NDs in the end-up orientation on the streptavidin crystal plane using biotin-labeled samples. Although it is difficult to further elucidate the molecular mechanisms of Sec translocation machinery owing to the resolution of the HS-AFM observation system, nanodisc systems may allow the observation of protein

Figure 1. SecYEG-NDs and SecYAEG-NDs Fixed on Streptavidin Two-Dimensional Crystals in the End-Up Orientation

(A) HS-AFM image of SecYEG-NDs on streptavidin two-dimensional (SA 2D) crystals.

(B) Height distribution of SecYEG-NDs (left). The original maximum heights of SecYEG-NDs on SA 2D crystals were obtained from their cross-sectional profiles. The actual heights of SecYEG-NDs were calculated by subtracting the background (the median height of the lattice surface not containing holes of SA 2D crystals) estimated from a cross-sectional analysis. The red line represents the single-Gaussian fitting curve (7.7 ± 0.6 nm; n = 277, 277 molecules). Schematic illustration of SecYEG-NDs fixed on SA 2D crystals (orange lattice pattern) via biotin tags (right). The SecYEG-ND model was constructed based on the crystal structure of SecYEG (PDB: 5AWW) and the model of nanodisc including membrane scaffold proteins and lipids (PDB: 2MSC). The estimated height of SecYEG is indicated.

(C) HS-AFM image of SecYAEG-NDs on SA 2D crystal.

(D) Height distribution of SecYAEG-NDs (left). The blue line represents the single-Gaussian fitting curve (10.9 ± 0.8 nm; n = 305, 305 molecules). The actual heights of SecYAEG-NDs were calculated as in (B). Schematic illustration of SecYAEG-NDs fixed on SA 2D crystals using the crystal structure of the SecA-SecYEG complex (PDB: 3DIN) and nanodisc model (PDB: 2MSC).

(E) Three-dimensional images of (A) and (C).

(F) Simulated AFM image (right) of the SecYAEG-ND structure constructed by the model in (D) (left).

(G) Close-up view of HS-AFM images of SecYAEG-ND particles on SA 2D crystals, showing the fluctuation of the cytoplasmic domains of SecA.

See also Figures S1 and S2.

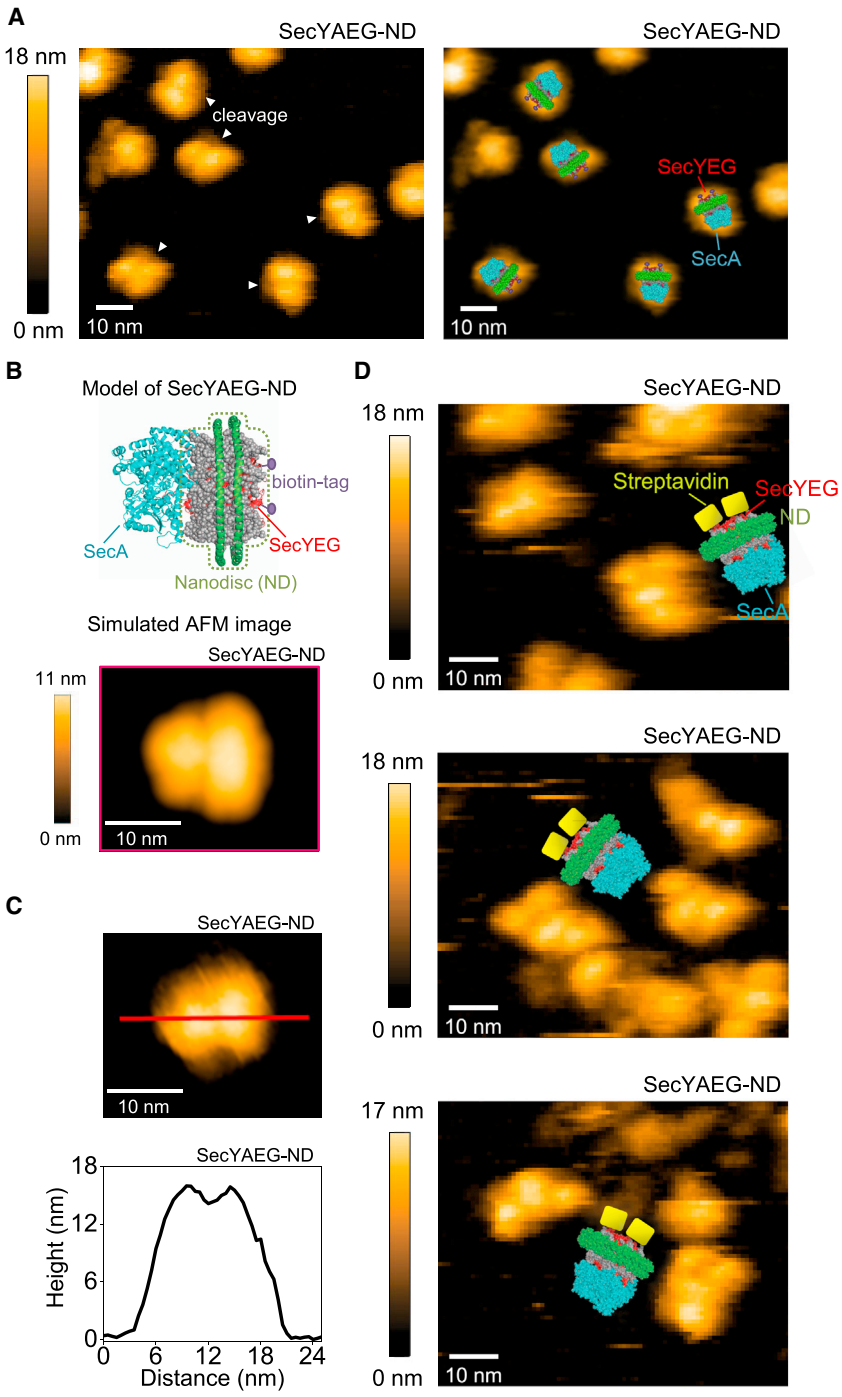

Figure 2. SecYAEG-NDs Loaded on the Mica Surface in the Side-On Orientation

(A) HS-AFM image of SecYAEG-NDs on the mica surface (left). Cleavages (indicated by white arrows) show the interface between SecA and the nanodisc. The SecYAEG-ND models in (B) are fitted to the observed particles (right).

(B) Simulated AFM image of the SecYAEG-ND model.

(C) Magnified AFM image of SecYAEG-NDs (top) and cross-sectional profiles shown along the red line drawn in the upper image (bottom).

(D) HS-AFM image of streptavidin-attached SecYAEG-NDs via biotin tags.

transport reactions across the membrane from at least two directions.

MgtE-NDs in the End-Up Orientation

Next, to address whether the system using nanodiscs is applicable to other membrane proteins, we applied this approach to the Mg^{2+} transporter MgtE. Dimeric MgtE regulates Mg^{2+} uptake into the cells in response to Mg^{2+} concentrations in the cytoplasm (Hattori et al., 2007, 2009; Ishitani et al., 2008). When the Mg^{2+} concentration in the cytoplasm is low, the assembly of the cytoplasmic region, consisting of N and CBS domains, weakens, inducing structural changes in the transmembrane domain for Mg^{2+} transport. In contrast, when sufficient Mg^{2+} exists, the cytoplasmic region is tightly packed, blocking Mg^{2+} uptake. We purified dimeric MgtE labeled with biotin on the periplasmic loop using a cysteine mutant (Figure S2) and observed MgtE-reconstituted nanodiscs (MgtE-NDs) anchored onto the streptavidin crystal in the presence of Mg^{2+} (Figures 3A–3C and Video S1). The HS-AFM images showed spherical structures, consistent with the simulated AFM image based on the crystal structure (Hattori et al., 2007). The highest region (average height = 9.6 ± 1.0 nm; n = 2,576, 24 molecules) in the center of the nanodisc is considered the dimeric MgtE, consistent with the estimated height. During the observation, the height of the MgtE-NDs was nearly constant (Figures 3D and 3E), suggesting that MgtE in nanodiscs in solution in the presence of Mg^{2+} was a hard, compact spherical structure, similar to the crystal structure. In contrast, the HS-AFM images of MgtE-NDs in the absence of Mg^{2+} showed a jagged topography, indicating that the cytosolic domains are constantly fluctuating (Figures 3F and 3G; Video S2). In the absence of Mg^{2+}, the height distribution showed two peaks, which were fitted using two Gaussian curves (Figure 3H). Although the larger average height (10.4 ± 2.0 nm; n = 2,156, 21 molecules) was approximately similar to the peak observed in the presence of Mg^{2+} (Figure 3E), the distribution became broader compared with that in the presence of Mg^{2+} (Figures 3E and 3H). The peak at 7.8 ± 0.5 nm corresponds to the height of MgtE-ND without CBS domains (7.4 nm), presumably due to the fluctuation of the cytoplasmic domains, including CBS domains. These phenomena of the cytoplasmic region observed by HS-AFM in the absence of Mg^{2+} were consistent with the flexibility of the N and CBS domains, which are distant from each other in the crystal structure and easily dissociated without Mg^{2+} (Hattori

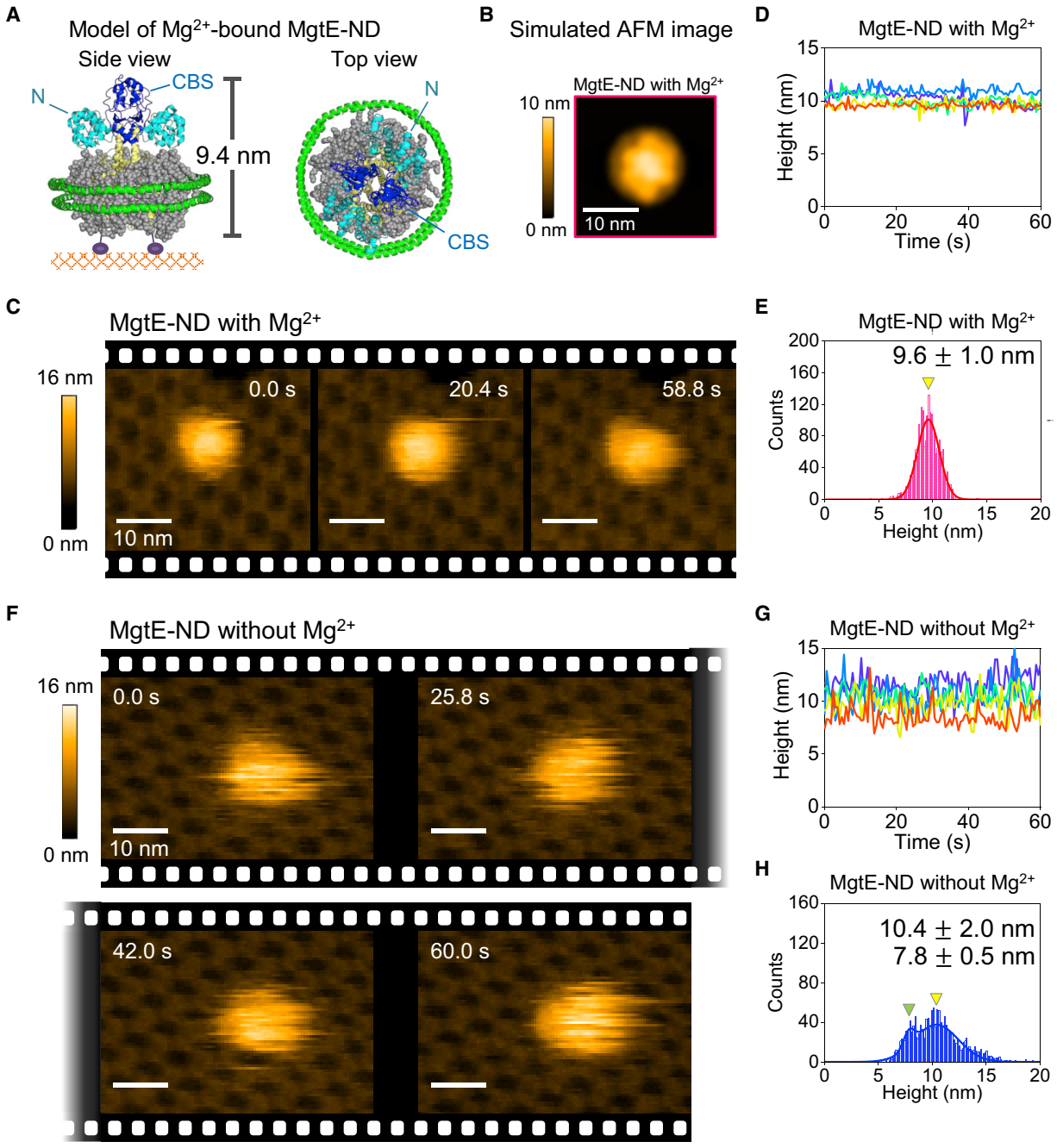

Figure 3. Fluctuation of MgtE-NDs in the End-Up Orientation, Depending on Mg^{2+}

(A) Mg^{2+}-bound MgtE-ND models constructed based on the crystal structure of MgtE (PDB: 2YVX) and the nanodisc model (PDB: 2MSC). The N and CBS domains are shown in cyan and blue, respectively. Side view showing a schematic illustration of MgtE-NDs fixed on SA 2D crystals via biotin tags. The estimated height of MgtE is shown.

(B) Simulated AFM image of the Mg^{2+}-bound MgtE-ND model, as shown in (A) (right).

(C) Successive AFM images of Mg^{2+}-bound MgtE-NDs on SA 2D crystals.

(D) Time course of the height of five independent particles of Mg^{2+}-bound MgtE-NDs.

(E and F) Height distribution of Mg^{2+}-bound MgtE-NDs (E). The red line represents the single-Gaussian fitting curve (9.6 ± 1.0 nm; n = 2,576, 24 molecules). The original maximum heights of MgtE-NDs on SA 2D crystals were the highest point within the particle images of each frame. The actual heights were calculated by subtracting the background (the highest point within the SA 2D crystals images for each frame). (F) Successive AFM images of Mg^{2+}-unbound MgtE-NDs on SA 2D crystals.

(G) Time course of the height of five independent particles of Mg^{2+}-unbound MgtE-NDs.

(H) Height distribution of Mg^{2+}-unbound MgtE-NDs. The blue line represents the two Gaussian fitting curves (10.4 ± 2.0 nm and 7.8 ± 0.5 nm; n = 2,156, 21 molecules). The actual heights were calculated as in (E).

See also Figure S2; Videos S1 and S2.

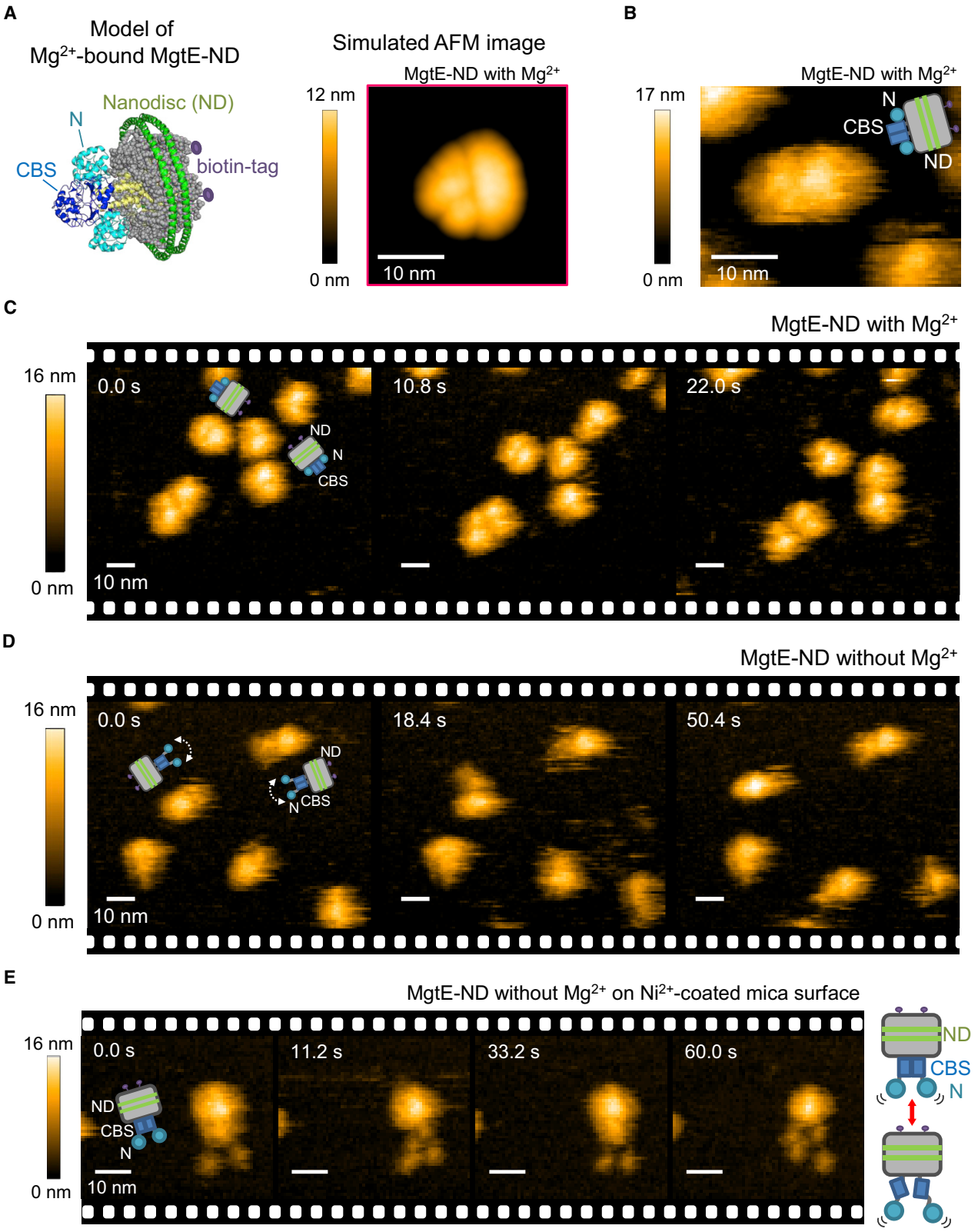

Figure 4. MgtE-NDs Placed on the Mica Surface in the Side-On Orientation in the Presence and Absence of Mg^{2+}

(A) Side view of the MgtE-ND model (left). Simulated AFM image of the MgtE-ND model (right).

(B) Magnified Mg^{2+}-bound MgtE-ND particles on the mica surface.

(legend continued on next page)

et al., 2007, 2009; Ishitani et al., 2008). Thus, we could place MgtE-reconstituted nanodiscs in the end-up orientation, similar to SecYAEG-reconstituted nanodiscs, and detect real-time fluctuations in the cytoplasmic domain of MgtE in nanodiscs.

MgtE-NDs in the Side-On Orientation

We next observed images of MgtE-NDs adsorbed on mica. All particles showed the elliptical nanodisc architecture not related to the Mg^{2+} concentration, whereas the cytoplasmic domains appeared different depending on the presence of Mg^{2+} (Figures 4C and 4D; Videos S3 and S4). We recognized the tightly assembled N and CBS domains in the presence of Mg^{2+}, consistent with the simulated AFM image of the crystal structure (Figures 4A–4C). In contrast, in the absence of Mg^{2+}, the cytoplasmic regions were highly flexible and ambiguous (Figure 4D). These observations are also consistent with the aforementioned results using the two-dimensional crystal. Additionally, we observed MgtE-NDs on the Ni^{2+}-coated mica surface, which is positively charged, strengthening the interaction between the negatively charged cytoplasmic region and the Ni^{2+}-coated mica (Figure 4E and Video S5). The HS-AFM images showed clearer cytoplasmic regions in the absence of Mg^{2+}, and successive images demonstrated the association (e.g., at 0.0 and 33.2 s) and disassembly (e.g., at 11.2 and 60.0 s) of the N and CBS domains in solution. Using HS-AFM, we observed the flexibility of the cytoplasmic domain of MgtE from two controlled directions in real time.

DISCUSSION

In this study, we employed nanodiscs containing membrane proteins that were biotin labeled via introduced cysteine residues for HS-AFM observation. By optimizing the supporting surface, membrane protein-embedded nanodiscs were immobilized to the end-up or side-on orientation in a well-controlled manner. The streptavidin crystal surface can specifically and tightly bind to biotin and prevent other nonspecific interactions, thereby allowing for the imaging of uniform particles in the end-up orientation. The mica surface enabled us to observe the membrane protein-embedded nanodiscs in the side-on orientation. The nanodisc lipid surface in the side-on orientation was vertically fixed on the mica surface, although the hydrophilic head groups of lipids are likely to favor interactions with the hydrophilic mica surface. The biotin label and large cytoplasmic region of the membrane protein protruding at both nanodisc lipid surfaces could prevent interactions between the lipid bilayer and the mica surface reported in previous studies (Koch et al., 2016; Zocher et al., 2012). This combination of HS-AFM and nanodisc technologies enabled us to observe real-time, dynamic structural changes in membrane proteins in the lipid environment from two distinct orientations. This method can be used for the dynamic imaging of other membrane proteins with a large cytoplasmic region, such as ABC transporters and receptor tyrosine kinases (Endres et al., 2014; Thomas and Tampe, 2018). Moreover, drastic conformational transitions in the soluble domains of membrane proteins could be inferred from static snapshots obtained by crystallography and electron micrography (Gutmann et al., 2018; Ho et al., 2018; Menting et al., 2013; Mi et al., 2017), and real-time movies such as HS-AFM observation provide complementary dynamic information regarding the molecular mechanism underlying membrane protein functions. In addition, this method can be applied to elucidate the dynamics of inherently disordered soluble regions of membrane proteins. Thus, this strategy may have applications in the analysis of important biological processes involving membrane protein dynamics to help understand their molecular mechanism in detail.

STAR★METHODS

Detailed methods are provided in the online version of this paper and include the following:

- KEY RESOURCES TABLE
- EXPERIMENTAL MODEL AND SUBJECT DETAILS
- CONTACT FOR REAGENT AND RESOURCE SHARING
- METHOD DETAILS
  - Preparation of SecYEG/SecYAEG-reconstituted Nanodiscs
  - Preparation of MgtE-reconstituted Nanodiscs
  - HS-AFM Observation
  - Simulation of AFM Images
- QUANTIFICATION AND STATISTICAL ANALYSIS
- DATA AND SOFTWARE AVAILABILITY

SUPPLEMENTAL INFORMATION

Supplemental Information includes two figures and five videos and can be found with this article online at https://doi.org/10.1016/j.str.2018.09.005.

ACKNOWLEDGMENTS

We thank K. Abe and S. Suzuki for secretarial assistance and K. Kobayashi for technical support. This work was supported by the JSPS/MEXT KAKENHI (grant nos. JP26119007, JP26119003, JP26291023, JP18H02405, JP17H05669, JP17K19528, JP16K14713, JP15H01537, JP15K06972, JP15H04360, JP16H00830, JP16H00758, JP15H03540, and JP25112507), Mitsubishi Foundation, Noguchi Institute, Naito Foundation, Mochida Memorial Foundation for Medical and Pharmaceutical Research, CREST, JST (grant no. JPMJCR13M1), and PRESTO, JST (grant no. JPMJPR12L3). *T. thermophilus* DNA was provided by RIKEN BRC, which is participating in the National Bio-Resources Project of the MEXT, Japan.

AUTHOR CONTRIBUTIONS

T.H., Y.S., and T.T.: conceptualization, manuscript drafting, and investigation; T.H., Y.S., N.K., T.U., T.A., Y.T., H.K., and T.T.: methodology; H.K. and T.T.: supervision.

(C and D) Successive AFM images of MgtE-NDs on the mica surface with (C) and without (D) Mg^{2+}.
(E) Successive AFM images of MgtE-NDs on Ni^{2+}-coated mica surface without Mg^{2+}. Schematic illustration depicting conformational transitions in the cytoplasmic domain, containing N and CBS domains, of MgtE-NDs.
See also Videos S3, S4, and S5.

DECLARATION OF INTERESTS

The authors declare no competing interests.

Received: May 2, 2018
Revised: June 6, 2018
Accepted: September 18, 2018
Published: October 11, 2018

REFERENCES

Akimaru, J., Matsuyama, S., Tokuda, H., and Mizushima, S. (1991). Reconstitution of a protein translocation system containing purified SecY, SecE, and SecA from *Escherichia coli*. Proc. Natl. Acad. Sci. U S A *88*, 6545–6549.

Ando, T., Kodera, N., Takai, E., Maruyama, D., Saito, K., and Toda, A. (2001). A high-speed atomic force microscope for studying biological macromolecules. Proc. Natl. Acad. Sci. U S A *98*, 12468–12472.

Ando, T., Uchihashi, T., Kodera, N., Yamamoto, D., Miyagi, A., Taniguchi, M., and Yamashita, H. (2008). High-speed atomic force microscopy for nano-visualization of dynamic biomolecular processes. Prog. Surf. Sci. *83*, 337–437.

Bahatyrova, S., Frese, R.N., Siebert, C.A., Olsen, J.D., Van Der Werf, K.O., Van Grondelle, R., Niederman, R.A., Bullough, P.A., Otto, C., and Hunter, C.N. (2004). The native architecture of a photosynthetic membrane. Nature *430*, 1058–1062.

Bayburt, T.H., Grinkova, Y.V., and Sligar, S.G. (2002). Self-assembly of discoidal phospholipid bilayer nanoparticles with membrane scaffold proteins. Nano Lett. *2*, 853–856.

Chatzi, K.E., Sardis, M.F., Economou, A., and Karamanou, S. (2014). SecA-mediated targeting and translocation of secretory proteins. Biochim. Biophys. Acta *1843*, 1466–1474.

Daimon, Y., Iwama-Masui, C., Tanaka, Y., Shiota, T., Suzuki, T., Miyazaki, R., Sakurada, H., Lithgow, T., Dohmae, N., Mori, H., et al. (2017). The TPR domain of BepA is required for productive interaction with substrate proteins and the beta-barrel assembly machinery complex. Mol. Microbiol. *106*, 760–776.

Endres, N.F., Barros, T., Cantor, A.J., and Kuriyan, J. (2014). Emerging concepts in the regulation of the EGF receptor and other receptor tyrosine kinases. Trends Biochem. Sci. *39*, 437–446.

Fotiadis, D., Liang, Y., Filipek, S., Saperstein, D.A., Engel, A., and Palczewski, K. (2003). Atomic-force microscopy: rhodopsin dimers in native disc membranes. Nature *421*, 127–128.

Gutmann, T., Kim, K.H., Grzybek, M., Walz, T., and Coskun, U. (2018). Visualization of ligand-induced transmembrane signaling in the full-length human insulin receptor. J. Cell Biol. *217*, 1643–1649.

Hattori, M., Tanaka, Y., Fukai, S., Ishitani, R., and Nureki, O. (2007). Crystal structure of the MgtE Mg^{2+} transporter. Nature *448*, 1072–1075.

Hattori, M., Iwase, N., Furuya, N., Tanaka, Y., Tsukazaki, T., Ishitani, R., Maguire, M.E., Ito, K., Maturana, A., and Nureki, O. (2009). Mg^{2+}-dependent gating of bacterial MgtE channel underlies Mg^{2+} homeostasis. EMBO J. *28*, 3602–3612.

Ho, H., Miu, A., Alexander, M.K., Garcia, N.K., Oh, A., Zilberleyb, I., Reichelt, M., Austin, C.D., Tam, C., Shriver, S., et al. (2018). Structural basis for dual-mode inhibition of the ABC transporter MsbA. Nature *557*, 196–201.

Ishitani, R., Sugita, Y., Dohmae, N., Furuya, N., Hattori, M., and Nureki, O. (2008). Mg^{2+}-sensing mechanism of Mg^{2+} transporter MgtE probed by molecular dynamics study. Proc. Natl. Acad. Sci. U S A *105*, 15393–15398.

Koch, S., de Wit, J.G., Vos, I., Birkner, J.P., Gordiichuk, P., Herrmann, A., van Oijen, A.M., and Driessen, A.J. (2016). Lipids activate SecA for high affinity binding to the SecYEG complex. J. Biol. Chem. *291*, 22534–22543.

Kodera, N., Yamamoto, D., Ishikawa, R., and Ando, T. (2010). Video imaging of walking myosin V by high-speed atomic force microscopy. Nature *468*, 72–76.

Kozai, T., Sekiguchi, T., Satoh, T., Yagi, H., Kato, K., and Uchihashi, T. (2017). Two-step process for disassembly mechanism of proteasome α7 homo-tetradecamer by α6 revealed by high-speed atomic force microscopy. Sci. Rep. *7*, 15373.

Mazhab-Jafari, M.T., Marshall, C.B., Smith, M.J., Gasmi-Seabrook, G.M., Stathopulos, P.B., Inagaki, F., Kay, L.E., Neel, B.G., and Ikura, M. (2015). Oncogenic and RASopathy-associated K-RAS mutations relieve membrane-dependent occlusion of the effector-binding site. Proc. Natl. Acad. Sci. U S A *112*, 6625–6630.

Menting, J.G., Whittaker, J., Margetts, M.B., Whittaker, L.J., Kong, G.K., Smith, B.J., Watson, C.J., Zakova, L., Kletvikova, E., Jiracek, J., et al. (2013). How insulin engages its primary binding site on the insulin receptor. Nature *493*, 241–245.

Mi, W., Li, Y., Yoon, S.H., Ernst, R.K., Walz, T., and Liao, M. (2017). Structural basis of MsbA-mediated lipopolysaccharide transport. Nature *549*, 233–237.

Milhiet, P.E., Gubellini, F., Berquand, A., Dosset, P., Rigaud, J.L., Le Grimellec, C., and Levy, D. (2006). High-resolution AFM of membrane proteins directly incorporated at high density in planar lipid bilayer. Biophys. J. *91*, 3268–3275.

Miyagi, A., Chipot, C., Rangl, M., and Scheuring, S. (2016). High-speed atomic force microscopy shows that annexin V stabilizes membranes on the second timescale. Nat. Nanotechnol. *11*, 783–790.

Ngo, K.X., Kodera, N., Katayama, E., Ando, T., and Uyeda, T.Q. (2015). Cofilin-induced unidirectional cooperative conformational changes in actin filaments revealed by high-speed atomic force microscopy. Elife *4*, e04806.

du Plessis, D.J., Nouwen, N., and Driessen, A.J. (2011). The Sec translocase. Biochim. Biophys. Acta *1808*, 851–865.

Rapoport, T.A., Li, L., and Park, E. (2017). Structural and mechanistic insights into protein translocation. Annu. Rev. Cell Dev. Biol. *33*, 369–390.

Rouck, J.E., Krapf, J.E., Roy, J., Huff, H.C., and Das, A. (2017). Recent advances in nanodisc technology for membrane protein studies (2012-2017). FEBS Lett. *591*, 2057–2088.

Ruan, Y., Miyagi, A., Wang, X., Chami, M., Boudker, O., and Scheuring, S. (2017). Direct visualization of glutamate transporter elevator mechanism by high-speed AFM. Proc. Natl. Acad. Sci. U S A *114*, 1584–1588.

Seelert, H., Poetsch, A., Dencher, N.A., Engel, A., Stahlberg, H., and Muller, D.J. (2000). Structural biology. Proton-powered turbine of a plant motor. Nature *405*, 418–419.

Shibata, M., Yamashita, H., Uchihashi, T., Kandori, H., and Ando, T. (2010). High-speed atomic force microscopy shows dynamic molecular processes in photoactivated bacteriorhodopsin. Nat. Nanotechnol. *5*, 208–212.

Shibata, M., Nishimasu, H., Kodera, N., Hirano, S., Ando, T., Uchihashi, T., and Nureki, O. (2017). Real-space and real-time dynamics of CRISPR-Cas9 visualized by high-speed atomic force microscopy. Nat. Commun. *8*, 1430.

Sugano, Y., Furukawa, A., Nureki, O., Tanaka, Y., and Tsukazaki, T. (2017). SecY-SecA fusion protein retains the ability to mediate protein transport. PLoS One *12*, e0183434.

Sumino, A., Uchihashi, T., and Oiki, S. (2017). Oriented reconstitution of the full-length KcsA potassium channel in a lipid bilayer for AFM imaging. J. Phys. Chem. Lett. *8*, 785–793.

Tanaka, Y., Sugano, Y., Takemoto, M., Mori, T., Furukawa, A., Kusakizako, T., Kumazaki, K., Kashima, A., Ishitani, R., Sugita, Y., et al. (2015). Crystal structures of SecYEG in lipidic cubic phase elucidate a precise resting and a peptide-bound state. Cell Rep. *13*, 1561–1568.

Taufik, I., Kedrov, A., Exterkate, M., and Driessen, A.J. (2013). Monitoring the activity of single translocons. J. Mol. Biol. *425*, 4145–4153.

Thomas, C., and Tampe, R. (2018). Multifaceted structures and mechanisms of ABC transport systems in health and disease. Curr. Opin. Struct. Biol. *51*, 116–128.

Tsirigotaki, A., De Geyter, J., Sostaric, N., Economou, A., and Karamanou, S. (2017). Protein export through the bacterial sec pathway. Nat. Rev. Microbiol. *15*, 21–36.

Tsukazaki, T. (2018). Structure-based working model of SecDF, a proton-driven bacterial protein translocation factor. FEMS Microbiol. Lett. *365*, https://doi.org/10.1093/femsle/fny112.

Tsukazaki, T., Mori, H., Fukai, S., Ishitani, R., Mori, T., Dohmae, N., Perederina, A., Sugita, Y., Vassylyev, D.G., Ito, K., et al. (2008). Conformational transition of Sec machinery inferred from bacterial SecYE structures. Nature *455*, 988–991.

Uchihashi, T., Iino, R., Ando, T., and Noji, H. (2011). High-speed atomic force microscopy reveals rotary catalysis of rotorless F_1-ATPase. Science *333*, 755–758.

Uchihashi, T., Kodera, N., and Ando, T. (2012). Guide to video recording of structure dynamics and dynamic processes of proteins by high-speed atomic force microscopy. Nat. Protoc. *7*, 1193–1206.

Vassylyev, D.G., Mori, H., Vassylyeva, M.N., Tsukazaki, T., Kimura, Y., Tahirov, T.H., and Ito, K. (2006). Crystal structure of the translocation ATPase SecA from Thermus thermophilus reveals a parallel, head-to-head dimer. J. Mol. Biol. *364*, 248–258.

Yamamoto, D., Nagura, N., Omote, S., Taniguchi, M., and Ando, T. (2009). Streptavidin 2D crystal substrates for visualizing biomolecular processes by atomic force microscopy. Biophys. J. *97*, 2358–2367.

Zimmer, J., Nam, Y., and Rapoport, T.A. (2008). Structure of a complex of the ATPase SecA and the protein-translocation channel. Nature *455*, 936–943.

Zocher, M., Roos, C., Wegmann, S., Bosshart, P.D., Dotsch, V., Bernhard, F., and Muller, D.J. (2012). Single-molecule force spectroscopy from nanodiscs: an assay to quantify folding, stability, and interactions of native membrane proteins. ACS Nano *6*, 961–971.

STAR★METHODS

KEY RESOURCES TABLE

REAGENT or RESOURCE	SOURCE	IDENTIFIER
Bacterial and Virus Strains		
BL21(DE3)	Laboratory stock	N/A
Rosetta2(DE3)	Novagen	Cat# 71397
Chemicals, Peptides, and Recombinant Proteins		
n-dodecyl-β-D-maltopyranoside (DDM)	Glycon	Cat# D97002
Biotin-PEAC$_5$-maleimide	Dojindo	Cat# 344-06391
MSP1D1	Laboratory stock	N/A
E. coli Total Lipid Extract	Avanti Polar Lipids	Cat# 100500
Bio-Beads SM-2 Adsorbents	BIO-RAD	Cat# 1528920
TEV protease	Laboratory stock	N/A
Recombinant DNA		
Plasmid : Vector pTV118N	Takara Shuzo	Cat# 3328
Plasmid : Vector pACYCDuet-1	Novagen	Cat# 71147-3
Plasmid : Vector pET-16b	Daimon et al., 2017	N/A
pTT610 (pTV118N-based vector)	Addgene	Cat# 101742
pAK24 (pACYCDuet-1-based vector)	Addgene	Cat# 101741
T. thermophilus mgtE	RIKEN BRC	Cat# JCM 10941
Software and Algorithms		
Kodec 4.5.7.22 (for cross-sectional analysis)	Kodera et al., 2010	N/A
Origin 2018 (for a graph creation and Gaussian fitting)	OriginLab	https://www.originlab.com/
Pymol 2.0 (to draw a model of membrane protein-embedded in nanodisc)	https://www.pymol.org/	N/A
IgorPro 6.36 (for high-speed AFM analysis)	WaveMetrics	https://www.wavemetrics.com/
Deposited Data		
SecYEG crystal structure	Tanaka et al., 2015	PDB: 5AWW
SecA-SecYEG crystal structure	Zimmer et al., 2008	PDB: 3DIN
Model of nanodisc including membrane scaffold proteins and lipids	Mazhab-Jafari et al., 2015	PDB: 2MSC
MgtE crystal structure	Hattori et al., 2007	PDB: 2YVX
Other		
Laboratory-built high-speed AFM	Ando et al., 2001, 2008; Uchihashi et al., 2012	N/A

EXPERIMENTAL MODEL AND SUBJECT DETAILS

Each *E. coli* transformant altered from the *E. coli* strains BL21 (DE3) (Laboratory stock) and Rosetta 2(DE3) (Novagen, Darmstadt, Germany) was isolated and stored in LB media containing 20% glycerol at −80°C as a glycerol stock.

CONTACT FOR REAGENT AND RESOURCE SHARING

Further information and requests for reagents may be directed to, and will be fulfilled by the Lead Author, Tomoya Tsukazaki (ttsukazaki@mac.com).

METHOD DETAILS

Preparation of SecYEG/SecYAEG-reconstituted Nanodiscs

Mutations in *secY* of pAK24 and pTT610 were introduced by site-directed mutagenesis. The resulting plasmids encoded SecY(L2V, S148C, R208C, R252G)-His_6, SecE, and SecG and SecY(L2V, S148C, R208C, R252G)-$(GGSG)_4$-$SecA(C648S)_{1-939}$-His_{10}, SecE, and SecG, respectively. SecYEG was purified, as described previously (Tanaka et al., 2015). SecYAEG was prepared by Ni-NTA column chromatography, as described previously (Sugano et al., 2017). After decreasing the concentration of NaCl to 50 mM using an Amicon Ultra filter (Ultra-15, MWCO 100 kDa; Merck Millipore, Darmstadt, Germany), a reductant, β-mercaptoethanol (β-ME), was added to the protein solution with 15 mM. To remove the reductant, the reduced protein solution was purified using a HiTrap SP HP column (GE Healthcare, Chicago, IL, USA) (Sugano et al., 2017). Biotin-$PEAC_5$-maleimide (Dojindo, Kumamoto, Japan) dissolved in dimethyl sulfoxide was added to the purified protein at a molar ratio of Biotin-$PEAC_5$-maleimide:SecYEG = 20:1. The solution was incubated at room temperature for 1 h and then at 4°C for 12 h. To remove excess Biotin-$PEAC_5$-maleimide, the SecYEG and SecYAEG solutions were loaded on a Superdex 200 Increase 5/150 GL column and a Superose 6 Increase 10/300 GL column (GE Healthcare), respectively, equilibrated with a buffer (20 mM Tris-HCl [pH 8.0], 300 mM NaCl, 5% glycerol, and 0.1% *n*-dodecyl-β-D-maltoside [DDM]). The labeled Sec complex was reconstituted into nanodiscs as described previously (Sugano et al., 2017).

Preparation of MgtE-reconstituted Nanodiscs

The *mgtE* gene from *T. thermophilus* was cloned into modified pET16b (Daimon et al., 2017) and mutated by site-directed mutagenesis. The resulting plasmid, encoding MG-His_{10}-SSGENLYFQGSH-MgtE(A312C), was introduced into *Escherichia coli* strain Rosetta 2(DE3) (Novagen, Darmstadt, Germany). The transformants were cultivated at 37°C to an A600 of approximately 0.7 in LB medium supplemented with 50 μg/mL ampicillin and 20 μg/mL chloramphenicol. The expression of MgtE was induced with 0.5 mM isopropyl β-D-1-thiogalactopyranoside at 20°C for 16 h. The cells were harvested by centrifugation at 5000 × *g* for 10 min, and pellets were resuspended in a buffer (10 mM Tris-HCl [pH 8.0], 1 mM ethylenediaminetetraacetic acid and 0.1 mM phenylmethylsulfonyl fluoride [PMSF]) and disrupted by sonication with a Q500 Sonicator (QSONICA). After centrifugation at 25,000 × *g* for 30 min, the supernatant was ultracentrifuged (138,000 × *g* for 60 min at 4°C), and the membrane fraction was collected. The membrane fraction was solubilized in a buffer (50 mM HEPES-NaOH [pH 7.0], 300 mM NaCl, 20 mM imidazole, 1.5% DDM, and 0.1 mM PMSF). After ultracentrifugation (138,000 × *g* for 30 min at 4°C), the supernatant was mixed with Ni-NTA Agarose (Qiagen, Valencia, CA, USA) equilibrated with buffer A (50 mM HEPES-NaOH [pH 7.0], 300 mM NaCl, and 0.1% DDM) containing 20 mM imidazole for 30 min at 4°C. The resin was washed with buffer A containing 50 mM imidazole and then eluted with buffer A containing 300 mM imidazole. The His_{10} tag was cleaved by His-tagged TEV protease, and the sample was reloaded onto the Ni-NTA column equilibrated with buffer A containing 20 mM imidazole to remove the TEV protease. The flowthrough fraction was collected and β-ME was added to a final concentration of 15 mM. The mixture was concentrated using an Amicon Ultra filter (Ultra-4, MWCO 50 kDa; Merck Millipore) and loaded on a Superdex 200 Increase 10/300 GL column (GE Healthcare) equilibrated with buffer A. The labeling of Biotin-$PEAC_5$-maleimide was performed as described for SecYEG/SecYAEG preparation. The biotin-labeled protein solution was loaded on a Superdex 200 Increase 5/150 GL column equilibrated with buffer A.

The protein-lipid mixture containing 6.35 mg/mL biotin-labeled MgtE, 7.8 mg/mL MSP1D1 (a membrane scaffold protein), and 8 mg/mL *E. coli* phospholipids (Avanti) in buffer A was gently mixed at 4°C for 1 h. To remove the detergent, Bio-Beads SM2 (Bio-Rad, Hercules, CA, USA) were added to the mixture. After gently mixing at 4°C overnight, the mixture was filtered using Centrifugal Filters PVDF 0.22 μm (Millipore) and then loaded on a Superdex 200 Increase 10/300 GL column equilibrated with 50 mM HEPES-NaOH [pH 8.0] and 300 mM NaCl.

HS-AFM Observation

HS-AFM imaging of SecYEG-NDs, SecYAEG-NDs, and MgtE-NDs was performed using a laboratory-built HS-AFM, as previously described (Ando et al., 2001, 2008; Uchihashi et al., 2012). The HS-AFM was equipped with small cantilevers (BL-AC10DS-A2 or BL-AC7DS-KU4; Olympus, Tokyo, Japan) and operated in the tapping mode. The free oscillation amplitude was approximately 1.5 nm, and the set-point amplitude was 80–90% of the free amplitude. Imaging rate, scan size, and feedback parameters were optimized during observation to enable visualization with the minimum tip force.

Prior to observations of the SecYEG-NDs, SecYAEG-NDs, and MgtE-NDs on SA 2D crystals, streptavidin molecules were two-dimensionally crystallized on the mica surface as previously described (Yamamoto et al., 2009), except SA 2D crystals were formed within 15–30 min of incubation. SecYEG-NDs and SecYAEG-NDs were incubated for 5 min on SA 2D crystals after SecYEG-ND and SecYAEG-ND samples were diluted in buffer A (50 mM HEPES-NaOH [pH 7.0] and 300 mM NaCl). The surface of SA 2D crystals was then washed with buffer (A) HS-AFM imaging was performed in buffer A for SecYEG-NDs or buffer B (50 mM HEPES-NaOH [pH 7.0], 300 mM NaCl, and 100 mM KCl) for SecYAEG-NDs. To prepare Mg^{2+}-bound MgtE-NDs, purified MgtE-NDs were diluted in buffer C (50 mM HEPES-NaOH [pH 7.0], 300 mM NaCl, 100 mM KCl, and 50 mM $MgCl_2$), incubated for 5 min on SA 2D crystals, and then washed in buffer (C) HS-AFM observations were carried out in buffer (C) After imaging Mg^{2+}-bound MgtE-NDs, the surface was washed in buffer B, not including $MgCl_2$, to observe Mg^{2+}-unbound MgtE-NDs. HS-AFM imaging was performed in buffer (B)

For observation on mica, SecYAEG-NDs were incubated for 5 min on the mica surface after SecYAEG-ND samples were diluted into 50 mM HEPES-NaOH [pH 7.0] and 100 mM NaCl. The mica surface was then washed in 50 mM HEPES-NaOH [pH 7.0]. HS-AFM

imaging was carried out in 50 mM HEPES-NaOH [pH 7.0]. To address the orientation of SecYAEG-NDs on the mica surface, 100 nM streptavidin in 50 mM HEPES-NaOH [pH 7.0] and 100 mM NaCl was loaded on the mica surface after imaging SecYAEG-NDs. After incubation for 5 min, the surface was washed in 50 mM HEPES-NaOH [pH 7.0] and observed in 50 mM HEPES-NaOH [pH 7.0] using HS-AFM. To prepare Mg^{2+}-bound and Mg^{2+}-unbound MgtE-ND samples on mica, purified MgtE-NDs were diluted in 50 mM HEPES-NaOH [pH 7.0] with or without 50 mM $MgCl_2$. Mg^{2+}-bound and Mg^{2+}-unbound MgtE-NDs were incubated for 5 min on the mica surface and then washed in 50 mM HEPES-NaOH [pH 7.0] with or without 50 mM $MgCl_2$. HS-AFM imaging was carried out in 50 mM HEPES-NaOH [pH 7.0] with or without 50 mM $MgCl_2$. To observe the cytoplasmic domain of MgtE-NDs, Mg^{2+}-unbound MgtE-NDs were loaded on the mica surface coated with Ni^{2+} ion as follows. First, 100 mM $NiSO_4$ was deposited on the mica surface and incubated for 5 min. The surface was then successively washed in MilliQ water and 50 mM HEPES-NaOH [pH 7.0]. Mg^{2+}-unbound MgtE-NDs were incubated for 5 min on the Ni-coated mica surface and then washed in 50 mM HEPES-NaOH [pH 7.0]. HS-AFM observation was performed in 50 mM HEPES-NaOH [pH 7.0].

Simulation of AFM Images

Simulated AFM images of SecYAEG-NDs and MgtE-NDs were calculated using an AFM probe modeled by a cone shape with a radius of 0.5–1 nm and half cone of 10° as previously described (Kozai et al., 2017; Uchihashi et al., 2011). The source code for Igor Pro 6.36 (Wave Metrics Inc., Lake Oswego, OR, USA) is available on request. The structural models of SecYAEG-ND and MgtE-ND structures were manually constructed by incorporating the SecA-SecYEG crystal structure (PDB: 3DIN) and MgtE crystal structure (PDB: 2YVX) into the nanodisc model (PDB: 2MSC) (Mazhab-Jafari et al., 2015) using Pymol (Schrodinger). The calculated simulation images were smoothed by fast-Fourier transform frequency filtering (cut-off wavelength of 0.77–2.50 nm).

QUANTIFICATION AND STATISTICAL ANALYSIS

The single Gaussian curve or two Gaussian curves fitting was performed using Origin2018 (OriginLab, Northampton, MA, USA) to calculate the average height of molecules. N is the number of counted height data as described in figure legends of Figures 1 and 3.

DATA AND SOFTWARE AVAILABILITY

HS-AFM image acquisition and analysis in this paper was carried out by laboratory-developed software based on Igor Pro 6.36 (Wave Metrics Inc., Lake Oswego, OR, USA). The source codes are available upon reasonable request. Kodec 4.4.7.39 (the latest version of Kodec 4.5.7.22 for cross-sectional analysis), a HS-AFM image viewer, coded in Visual C# (Visual Studio 2010, Microsoft, USA) is available (Ngo et al., 2015).

Structure, Volume *27*

Supplemental Information

Single-Unit Imaging of Membrane Protein-Embedded Nanodiscs from Two Oriented Sides by High-Speed Atomic Force Microscopy

Takamitsu Haruyama, Yasunori Sugano, Noriyuki Kodera, Takayuki Uchihashi, Toshio Ando, Yoshiki Tanaka, Hiroki Konno, and Tomoya Tsukazaki

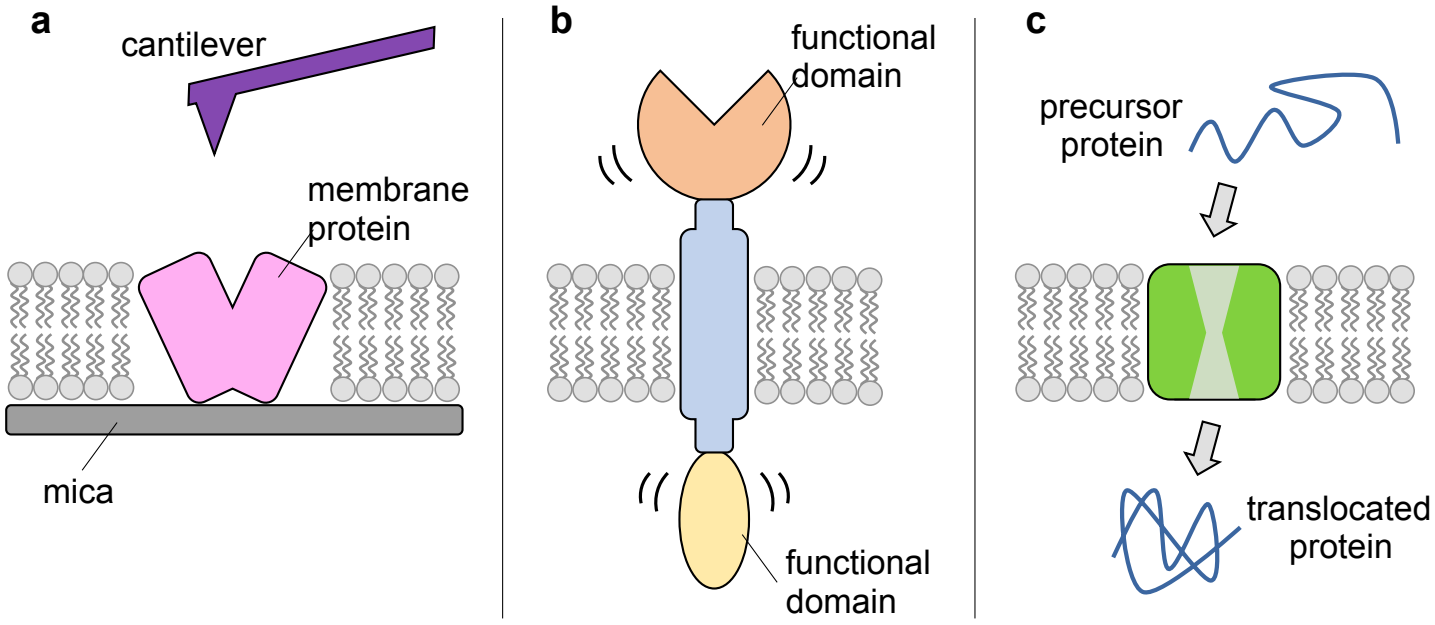

Figure S1. Schematic interpretation of typical membrane proteins embedded in the lipid bilayer, Related to Figure 1.
a, Conventional measurement of a membrane protein on the mica-supported lipid bilayer by AFM. The membrane protein directly interacts with the mica surface; observations from only one side of the membrane can be performed. **b**, A model of a membrane protein possessing functional domains on both sides of the membrane, such as certain kinases. Using the method described in **a**, the cooperative conformational changes on both sides of the membrane could not be observed at the same time. **c**, Diagram of protein translocation via a protein-conducting channel. To complete the protein translocation across the membrane, sufficient space is required on both sides of the membrane. Using the system in **a**, steric hindrance of the translocated protein hampers the translocation of the substrate protein.

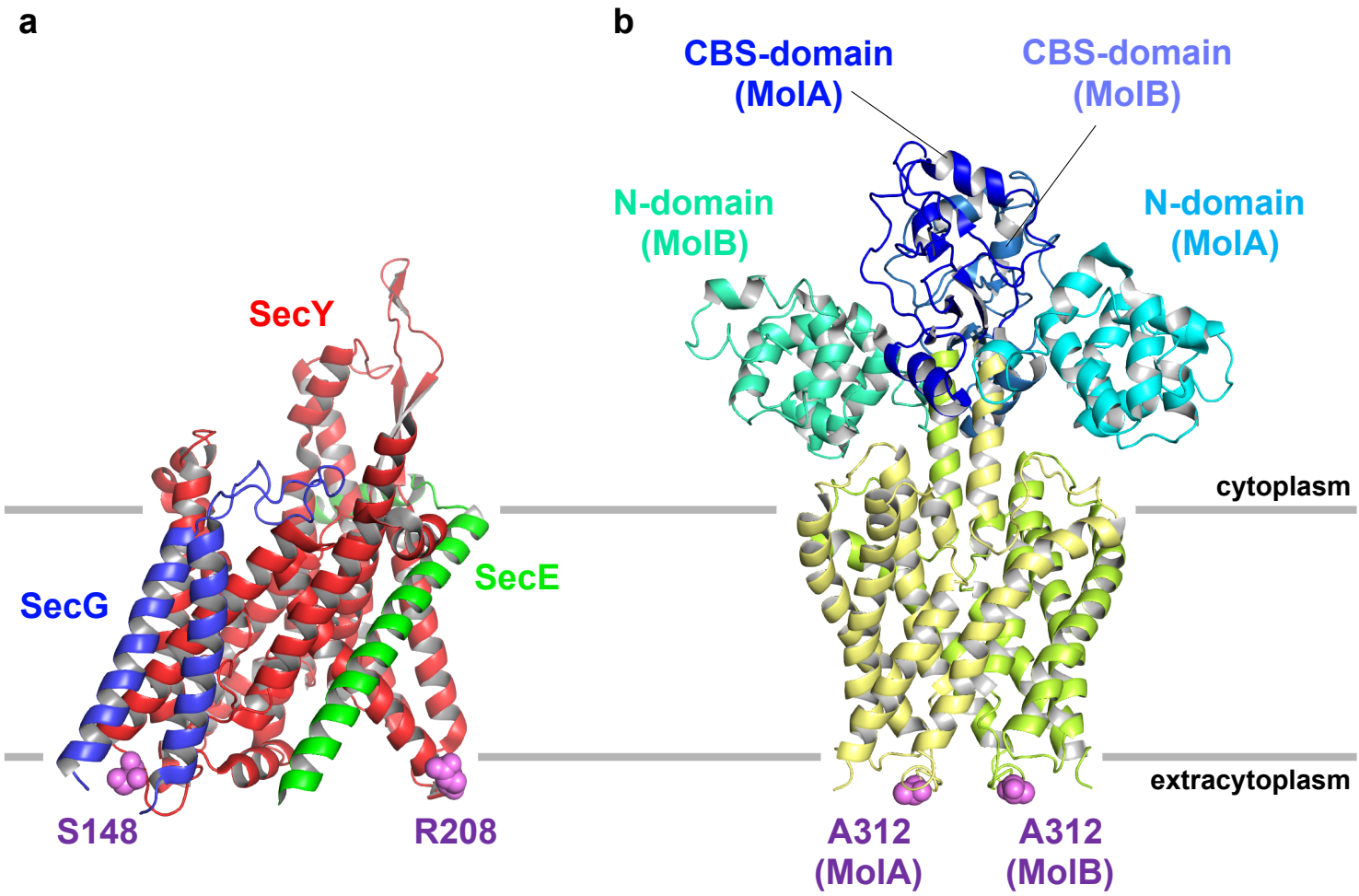

Figure S2. Positions of Cys mutations in the SecYEG complex and MgtE, Related to Figure 1 and 3.
a, Crystal structure of *T. thermophilus* SecYEG at 2.7 Å resolution (PDB: 5AWW). **b**, Crystal structure of dimeric MgtE in the presence of Mg^{2+} (PDB: 2YVX). The spheres (violet) show the positions of cysteine substitution for biotin labeling.